Data Article

Ruthenium under ultrafast laser excitation: Model and dataset for equation of state, conductivity, and electron-ion coupling

Yu. Petrov [a, b], K. Migdal [c], N. Inogamov [a, d], V. Khokhlov [a],
D. Ilnitsky [c], I. Milov [e, *], N. Medvedev [f, g], V. Lipp [h],
V. Zhakhovsky [c, d]

[a] Landau Institute for Theoretical Physics, Russian Academy of Sciences, Chernogolovka, 142432, Russia
[b] Moscow Institute of Physics and Technology, Institutskiy Pereulok 9, Dolgoprudny, Moscow Region, 141700, Russia
[c] Dukhov Research Institute of Automatics, Sushchevskaya 22, Moscow, 127055, Russia
[d] Joint Institute for High Temperatures, Russian Academy of Sciences, Izhorskaya 13 Bldg.2, Moscow, 125412, Russia
[e] Industrial Focus Group XUV Optics, MESA+ Institute for Nanotechnology, University of Twente, Drienerlolaan 5, 7522, NB Enschede, the Netherlands
[f] Institute of Physics, Czech Academy of Sciences, Na Slovance 2, 182 21, Prague 8, Czech Republic
[g] Institute of Plasma Physics, Czech Academy of Sciences, Za Slovankou 3, 182 00 Prague 8, Czech Republic
[h] Center for Free-Electron Laser Science CFEL, Deutsches Elektronen-Synchrotron DESY, Notkestrasse 85, 22607, Hamburg, Germany

ARTICLE INFO

ABSTRACT

Interaction of ultrashort laser pulses with materials can bring the latter to highly non-equilibrium states, where the electronic temperature strongly differs from the ionic one. The properties of such excited material can be considerably different from those in a hot, but equilibrium state. The reliable modeling of laser-irradiated target requires careful analysis of its properties in both regimes. This paper reports a procedure which provides the equations of state of ruthenium using density functional theory calculations. The obtained data are fitted with analytical functions. The constructed equations of state are applicable in the one- and two-temperature regimes and in a wide range of densities, temperatures and pressures. The electron thermal conductivity and electron-phonon coupling factor are also calculated. The obtained

analytical expressions can be used in two-temperature hydrody-namics modeling of Ru targets pumped by ultrashort laser pulses. The data is related to the research article "Similarity in ruthenium damage induced by photons with different energies: From visible light to hard X-rays" [1].

Specifications Table

|	
Subject	Condensed Matter Physics
Specific subject area	Equation of state, thermal conductivity and electron-phonon coupling of Ru in one- and two-temperature states
Type of data	Formulas and Figures
How data were acquired	DFT calculations using VASP and Elk codes
Data format	Raw and analyzed
Parameters for data collection	In our DFT calculations the maximum energy of one-electron wavefunctions was fixed at 400 eV, the density of the Monkhorst-Pack grid was set equal to $21 \times 21 \times 21$ and the number of empty electron levels per atom was equal to 32. We describe exchange and correlation functional with a simplified generalized gradient approximation (GGA). The initial lattice constants are $a = b = 2.68$ Å and $c = 1.5789\,a$ at $T_e = 1000$ K
Description of data collection	The data were collected by performing DFT calculations of hexagonal close-packed Ru using the parameters described above. The lattice constants and electron temperature were varied in order to obtain Ru properties at different thermo-mechanical and two-temperature conditions
Data source location	Industrial Focus Group XUV Optics, MESA + Institute for Nanotechnology, University of Twente, Drienerlolaan 5, 7522 NB Enschede, The Netherlands
Data accessibility	The raw data files are provided in Supplementary Materials. All other data are in this article
Related research article	I. Milov et al. "Similarity in ruthenium damage induced by photons with different energies: From visible light to hard X-rays", Appl. Surf. Sci. 501, 143973 (2020) [1]

Value of the Data
- The presented data describe the thermo-mechanical behavior of Ru crystal in one- and two-temperature regimes in a wide range of density, temperature and pressure.
- The data can be used in damage studies of Ru induced by various sources, such as photons, electrons and ions.
- The data can be used in fundamental studies of warm dense matter formation induced by high intensity ultrashort laser pulses.

1. Data

1.1. Ab-initio calculations of ruthenium properties

1.1.1. Role of deformation of an hcp cell and variation of density

A change of the c/a ratio (height to base length of a cell) in an hcp lattice is investigated in the two-temperature (2T) regime. For each considered value of T_e we performed two DFT calculations: one with a fixed c/a ratio and another one with a relaxed c/a ratio corresponding to an energy minimum of the lattice. Ions are at the absolute zero temperature in both calculations. We found that the energy
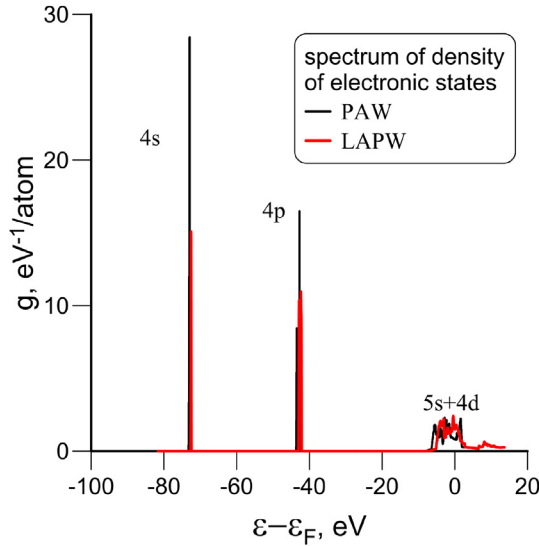
Fig. 1. DOS of Ru in the range of energies corresponding to the conduction and semicore electron bands. The black curve represents the result of a PAW calculation, while the DOS obtained in the LAPW approach is shown with the red curve. The raw data are provided in Supplementary Materials.

difference per atom between these calculations for each value of T_e is smaller than 0.1 eV. Constructing an equation of states for heated electrons we can neglect the effect of density variation on the electron pressure p_e and energy E_e.

Our decision not to conduct a series of quantum-mechanical calculations varying both the electron temperature T_e and the density can be justified with the following reason. The duration of the 2T stage is short (see Fig. 5 in the main text) due to a large value of the coefficient of electron-ion energy exchange (coupling parameter) in Ru. This duration is shorter than the acoustic timescale $t_s = d_T / c_s$, which is defined as the time necessary for a top of a rarefaction wave with speed c_s to pass a thickness d_T of a heated layer. During the 2T stage, there is no time for a significant decrease in density in the laser heated layer.

Nevertheless, the analytical formulas for P_e and E_e that we construct below take into account the density dependence, down to small values, in a *phenomenological* way based on a Fermi-gas approach. Of course, for small densities these expressions give us an order of magnitude prediction. But for moderate deviations from the normal density they are accurate. This is our way to avoid time and resources consuming DFT simulations for many different densities.

1.1.2. Energy expenses to ionize core electrons at high electron temperatures

The calculated DOS of Ru is shown in Fig. 1. There is a good agreement for the positions on the energy axis of the 4s and 4p semicore bands obtained by the PAW and LAPW approaches. Both methods predict these two bands to be located at 72 and 43 eV below the Fermi level, respectively. The values are close to the NIST data obtained using X-ray photoelectron spectroscopy: 75 eV for the 4s band and 43 eV for the 4p band (https://srdata.nist.gov/xps NIST X-ray Photoelectron Spectroscopy Database).

The electron heat capacity $C_e = \partial E_e / \partial T_e|_V$, shown in Fig. 2, is calculated from DFT simulations of the electron energy $E_e(T_e, \rho)$, obtained in Section 3.1. Below a temperature of $T_e \approx 2000$ K the heat capacity $C_e(T_e)$ rises linearly: $C_e \approx \gamma T_e$, where the slope is $\gamma = 400$ J/K^2/m^3 This slope is defined by the DOS in the vicinity of the Fermi level. The value of the slope γ for Ru is intermediate between the slopes $\sim 50-100$ J/K^2/m^3 for metals such as Al, Au, Ag and Cu and ten times higher slopes $\sim 500-1000$ J/K^2/m^3 for Ni or Pt.
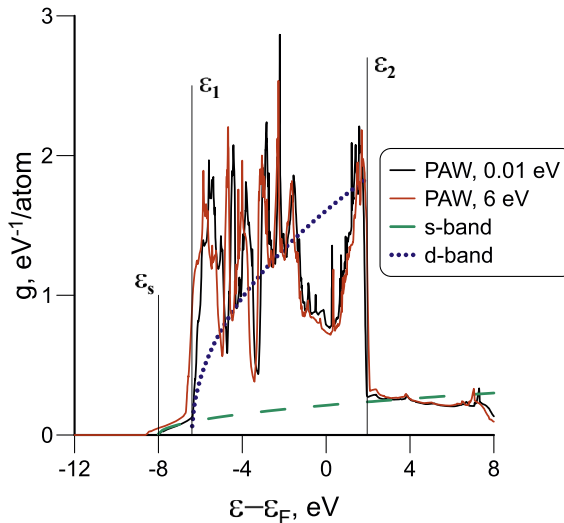
The Ru DOS in the conduction band is shown in Fig. 3. The electron spectrum obtained agrees well with the recent DFT simulations [4]. A discussion on the two-parabolic approximation presented in
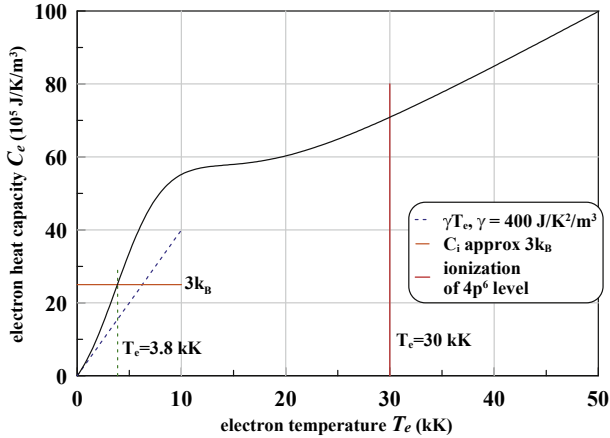
Fig. 2. Electron heat capacity C_e of Ru increases with electron temperature. At relatively small temperatures we have $C_e \propto T_e$. Linear growth of C_e slows down at $T_e \sim 10$ kK (the reasons are explained in the text). At higher temperatures $T_e \sim 20 - 30$ kK new growth of $C_e(T_e)$ begins. This growth appears thanks to ionization of 4p-electrons to the conduction band through a gap 43 eV. Similar behavior connected with ionization of a semicore shell was found for Al and W in Levashov et al. [2]. The raw data are provided in Supplementary Materials.

Fig. 3 is given below (Section 4.1). Here, the situation with the heat capacity is described. As stated before, the slope γ ($\gamma/\pi^2/k_B^2 = g(\varepsilon_F)/3$) is proportional to the density of electron states $g(\varepsilon = \varepsilon_F)$ at the Fermi level ε_F. The density of states $g(\varepsilon_F)$ is relatively high, if the upper edge ε_2 of the d-sub-band is above the Fermi energy.

Thus, for such d-metals as Au, Ag and Cu, having the edge $\varepsilon_2 < 0$ (i.e. below ε_F), the value of γ is smaller than in the cases with Ni or Pt, where $\varepsilon_2 > 0$. Ni and Pt have narrow d-bands and small ε_2 above

Fig. 3. DOS of Ru in the conduction band $4d^7 5s^1$. This is enlarged view of the band "5s+4d" shown in Fig. 1. Solid black and red lines correspond to the PAW calculations at $T_e = 0.01$ and 6 eV. Construction of the two-parabolic approximation of the electron spectrum is also shown. Green and blue curves represent the s- and d-parabolas, respectively. The bottom of the s-band and the edges of the d-band are marked as $\varepsilon_s = -8$ eV, $\varepsilon_1 = -6.4$ eV, and $\varepsilon_2 = +2$ eV, respectively. Two-parabolic approximation was presented previously for other metals in paper [3]. The raw data are provided in Supplementary Materials.

ε_F. Therefore they have extremely high values of γ. This peculiarity (intermediate value of γ) distinguishes Ru from other transition metals.

In the case of Ru, the linear growth of the heat capacity at relatively small temperature changes to saturation-like behavior above a temperature $T_e \sim 10$ kK, see Fig. 2. This is a general feature of all metals with $\varepsilon_2 > 0$. This saturation-like behavior is caused by a sharp decrease of the DOS for energies above ε_2, see Fig. 3. However, in the cases of d-metals with a d-band below ε_F (e.g., Au, Ag and Cu, where $\varepsilon_2 < 0$) the slope of the linear growth γT_e increases at T_e comparable to $|\varepsilon_2|$ due to "ionization" of d-electrons to energies above the Fermi level. The change of the $C_e(T_e)$ behavior for Ru from slow to active growth at $\sim 20-30$ kK is associated with excitation of 4p-electrons, see Fig. 2 (marked by the vertical red line). Thus, there are three regions of the function $C_e(T_e)$. First, we have a linear behavior $C_e \propto T_e$ in the electron temperature region $T_e \lesssim 10$ kK. In the second region $10 \lesssim T_e \lesssim 20 - 30$ kK the linear growth saturates. And in the third region $Te \gtrsim 20 - 30$ kK the growth of C_e with T_e increases steeper.

The gap between the 4p-band and the conduction band is wide, the number of excited electrons is small, but due to a large energy difference among the 4p and 5s+4d bands, the energy expenses for such ionization are significant. This circumstance increases the electron heat capacity in the third region. A similar behavior of the heat capacity C_e was observed in Ref. [2] for other metals.

2. Thermodynamics of the ion subsystem

2.1. Cold internal energy and pressures

Often the cold curve is defined by the given parameters: density at normal conditions, bulk modulus, sublimation energy, and Grüneisen parameter [5]. In our case we use another approach: the dependence of the hydrostatic pressure of the hcp Ru on the density is employed. This dependence is obtained with the DFT simulations described in Section 5.

We use a simple analytical approximation for the cold energy ε_i^{cold}. This approximation is based on two power law dependencies on the density (two-term approximation):

$$\varepsilon_i^{cold}(x) = A\left(x^a / a - x^b / b\right). \tag{1}$$

Then, the cold pressure $P_i^{cold} = -d\varepsilon_i^{cold}/dv$ is

$$P_i^{cold}(x) = (A / v_0)x\left(x^a - x^b\right). \tag{2}$$

In approximations (1) and (2) we have the normalized density $x = \rho/\rho_0 = v_0/v$, where ρ is the density, v is the volume per atom, $\rho_0 = 12.47$ g/cm^3 is the equilibrium density at zero temperature, v_0 is the volume per atom at $\rho = \rho_0$.

Fitting the cold curves to those obtained with the DFT calculation, we find

$$A = 3.81 \text{ a.u}, \quad a = 1.5886, \quad b = 1.3333, \tag{3}$$

where a.u. means atomic units. With the set of parameters (3), the cold energy and pressure become $\varepsilon_i^{cold} = 103.632 \, (x^a/a - x^b/b)$ eV per atom and $P_i^{cold} = 1230 \, x \, (x^a - x^b)$ GPa, respectively. Comparison of the DFT data and approximation (2) is shown in Fig. 4.

The difference between the DFT calculations presented here and the ones published in Ref. [4] shown in Fig. 4 stems from the different parameterizations of an exchange-correlations functional PW91. The Vanderbilt ultra-soft pseudopotential in Ref. [4] is another source of the discrepancy. This approach leads to a slightly underestimated value of the density at normal conditions, as seen in Fig. 4, since the goal of the paper [4] was to calculate the elastic and phonon properties of Ru. It should be mentioned also that a deviation in density within 5% is not unusual for DFT calculations.
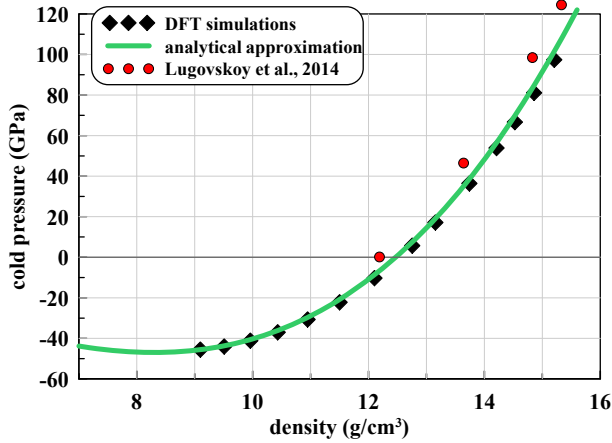
Fig. 4. Comparison of cold curves: the filled black rhombuses present our DFT data, the filled red circles are taken from DFT simulations given in Ref. [4], and the curve corresponds to the analytical approximation (2), (3). The raw data are provided in Supplementary Materials.

Fig. 5 shows the internal cold energies according to the two-term approximation (1), together with the five values of energies taken from the paper by Chelikowsky et al. [6] (Fig. 1 therein). We approximate these five values analytically with a two-term expression also shown in Fig. 5. Taking the derivative of this two-term approximation of the data from Ref. [6] with respect to the volume, we obtain an expression for the cold pressure corresponding to the paper [6]. A good agreement of our DFT data for the cold pressure and the approximation of the DFT data from Ref. [6] is shown in Fig. 6.

2.2. Hydrostatic versus uniaxial stretching - influence of crystallographic orientation

The cold ($T_e = 0$, $T_i = 0$) DFT data are shown with the black diamonds in Fig. 4. These data are obtained in the hydrostatic approximation, where we relax the parameter c/a for every value of the
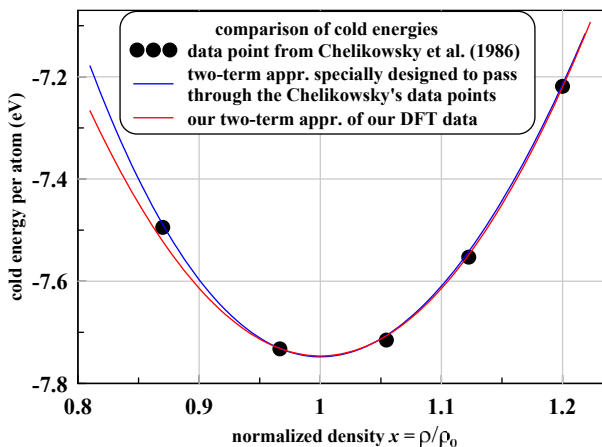
Fig. 5. Comparison of cold energies: our DFT data approximated by the two-term expression (1), (3) (the red continuous curve), the DFT data points (filled circles) taken from Ref. [6], and the two-term expression specially designed to fit the Chelikowsky's data point (the blue curve).
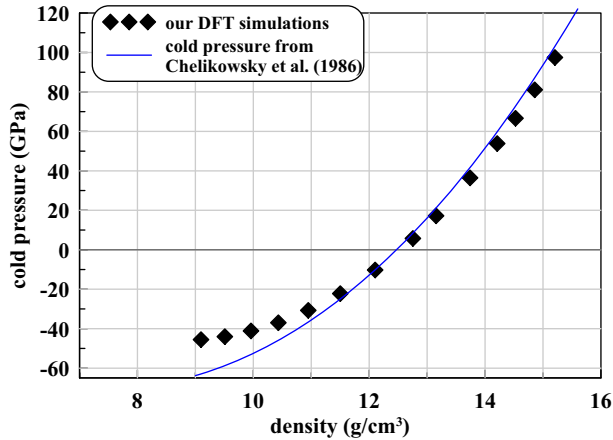
Fig. 6. Comparison of cold pressures: our DFT data (the black rhombuses) versus cold pressure obtained as derivative of cold energy thanks to the two-term approximation of the DFT data for cold energy from Ref. [6] (the blue curve); see also Figs. 4 and 5.

density. As a result of relaxation the parameter c/a achieves its equilibrium value corresponding to the setpoint density, which minimizes the cold energy.

In that minimum the stress tensor becomes isotropic and the shear stress equals to zero. Fig. 7 shows the relaxed values of the ratio c/a as a function of hydrostatic pressure in an hcp lattice. The difference between our calculations and those by Chelikowsky et al. [6] is caused by differences in the quantum mechanical approximations: in Ref. [6] the LDA (local density approximation) was used, while in our simulations we use the presumably more accurate GGA approach.

To estimate the influence of the ratio c/a on stress, we compare in Fig. 8 the hydrostatic pressures for the cases with relaxed and fixed ratios c/a. We see that the influence is very moderate.

2.3. Thermal addition to the internal energy and pressure of the ion subsystem

In the framework of the Mie-Grüneisen approach the ion internal energy per atom at the ion temperature T_i is presented as

$$\varepsilon_i(T_i, x) = A\left(x^a \big/ a - x^b \big/ b\right) + 3k_B T_i, \tag{4}$$
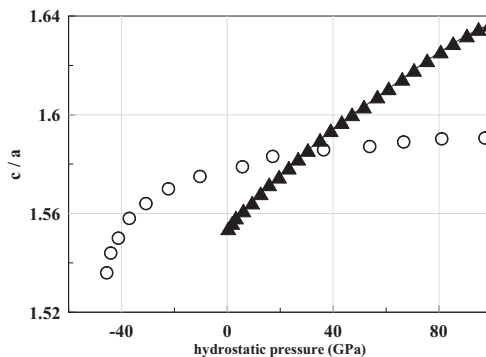
Fig. 7. Variation of the ratio c/a as a result of hydrostatic compression in cold Ru. Open circles represent our PAW calculations, while the earlier result by Chelikowsky et al. [6] are shown as filled triangles. The raw data are provided in Supplementary Materials.
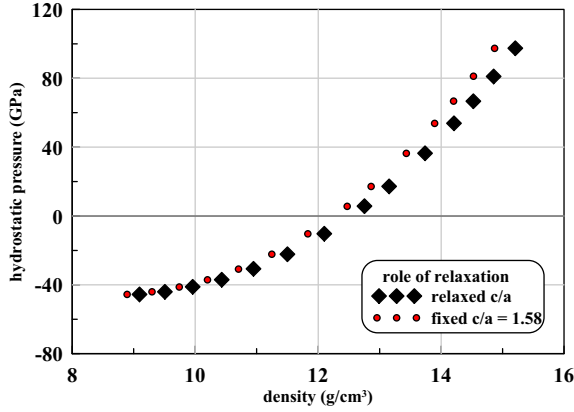
Fig. 8. Difference in hydrostatic pressures in the cases with relaxed and fixed ratios c/a. In the case with fixed ratio c/a the anisotropic stresses form as a result of compression or stretching. Hydrostatic pressure plotted here for this case is the sum $-(\sigma_{11} + \sigma_{22} + \sigma_{33})$. The raw data are provided in Supplementary Materials.

and the ion pressure is

$$P_i(T_i, x) = (A / v_0)x\left(x^a - x^b\right) + (3 / v_0)x\, G(x)\, k_B\, T_i. \tag{5}$$

In these expressions $G(x)$ is the Grüneisen parameter

$$G(x) = \mathrm{d}\ln\theta_D / \mathrm{d}\ln x \tag{6}$$

with $\theta_D(x)$ being the Debye temperature. The ion temperature dependent terms are added to the cold energy and pressure in order to take into account the change of the internal energy and pressure of the ion subsystem due to the heating.

The Debye temperature equals to

$$\theta_D(x) = \frac{\hbar}{k_B}c_s(x)\left(6\pi^2\frac{n}{2}\right)^{1/3}, \tag{7}$$

where $c_s(x)$ is the speed of sound, given by the expression

$$c_s(x) \propto \sqrt{dp_0/d\rho}.$$

Thus from the approximation (2) we have

$$c_s(x) \propto \sqrt{(a+1)x^a - (b+1)x^b}.$$

Using the expression for the Debye temperature (7) we obtain

$$\theta_D(x) \propto x^{1/3}\sqrt{(a+1)x^a - (b+1)x^b} \propto$$

$$\propto x^{1/3}\sqrt{y(x)}, \tag{8}$$

where x, as explained above, is a density ratio. In the expression (8) we introduced the designation

$$y(x) = \left((a+1)x^a - (b+1)x^b\right) \big/ (a-b).$$

Such expression for $y(x)$ leads to discontinuity in the Debye temperature (8) and the Grüneisen parameter (6), when the function $y(x)$ becomes negative at

$$x < \left(\frac{b+1}{a+1}\right)^{1/(a-b)}.$$

For this reason we change $y(x)$ to the positive at all values of x function

$$y_0(x) = \frac{(a+1)x^{2a+1}}{b+1+(a-b)x^{a+1}},\tag{9}$$

for which $y_0(1) = y(1)$, $y_0'(1) = y'(1)$, and $y(x)$ and $y_0(x)$ have the same asymptotic behavior at large x. Taking this into account, we replace $y(x)$ in (8) with $y_0(x)$ and write

$$\theta_D(x) \propto x^{1/3}\sqrt{y_0(x)}\tag{10}$$

instead of expression (8).

From (10) we obtain the expression for the density dependent Grüneisen parameter

$$G(x) = \frac{1}{3} + \frac{1}{2}\frac{d\ln y_0}{d\ln x} = \frac{1}{3} + \frac{1}{2}\frac{(2a+1)(b+1)+a(a-b)x^{a+1}}{b+1+(a-b)x^{a+1}},\tag{11}$$

which is used in our 2T-HD code. The dependence (11) is shown in Fig. 9.

Let's estimate value $G(x=1)$. It is known that

$$G = \beta\, B\, V_{mol}/c,$$

where $\beta = 3\cdot 6.4\cdot 10^{-6}$ K^{-1} is the thermal volume expansion coefficient, $V_{mol} = 8.1\cdot 10^{-6}$ m^3/mol is the molar volume, $c = 24.06$ J/(mol K) is the molar heat capacity. Values of the bulk modulus B vary in different sources [4,6,7], but can be estimated to the value $B = 320$ GPa. Using this value we obtain $G = 2.1$, which is close to our value $G(x=1) = 2.3$.
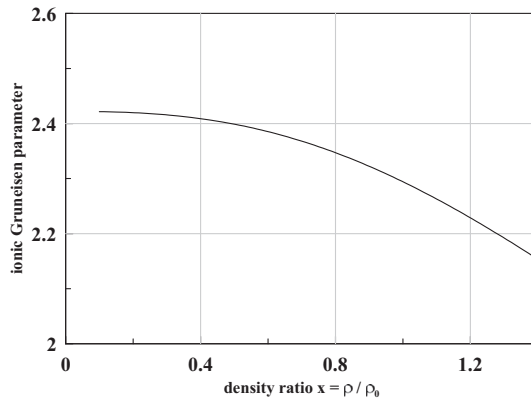

Fig. 9. Variation of the ion Grüneisen parameter with density according to expression (11).

3. Thermodynamics of the electron subsystem

3.1. Thermal addition to electron energy

Heat capacity of the electron subsystem is analyzed in Section 1.1.2 and in Fig. 2. Here we present a more general description including the pressure and internal energy increase due to heating of the electron subsystem. We introduce the electron energy E_e and electron pressure P_e as

$$E_e(T_e, x) = E(T_e, x) - E(T_e = 0, x), \tag{12}$$

$$P_e(T_e, x) = p(T_e, x) - p(T_e = 0, x). \tag{13}$$

In the definitions (12) and (13) we assume that the ion subsystem is cold. This means that ions are motionless and that they are fixed in their equilibrium positions in the lattice. Similar approaches were developed earlier for other metals [8]. The second terms in the definitions (12) and (13) are calculated not at $T_e = 0$, but at $T_e = 1000$ K. The value $T_e = 1000$ K is very small relative to the Fermi energy. Thus, these replacements introduce negligible changes.

Energy (12) and pressure (13) are calculated using the DFT approach described in Section 5. In these calculations we limit ourselves to the case of normal density Ru: $x = 1$, $x = \rho/\rho_0$. The dependence on variation of the density is introduced analytically employing the Fermi gas approximation. The unit cell height to base hexagonal ratio c/a was relaxed to its equilibrium value at every value of the electron temperature as is explained in Section 2.2.

The DFT calculations show that dependence of the Fermi energy of Ru on the compression and stretching is approximately consistent with that of $\varepsilon_F \propto x^{2/3}$ in our range of densities. This means that the effective mass of the s-electrons $m_s \simeq$ const in this range. Calculation based on the s-band parabola shown in Fig. 3 gives $m_s = 0.8 m_e$, where m_e is the free electron mass. The effective mass of s-electron is

$$m_s = \frac{\hbar^2}{2\varepsilon_{F0}} \left(3\pi^2 z_s n_i \right)^{2/3},$$

where ε_{F0} is the Fermi energy at $x = 1$, z_s is the number of s-electrons per atom, n_i is the concentration of ions.

Based on this assumption ($m_s \simeq$ const), we introduce a variable

$$\tau = 6\, k_B\, T_e \left/ \left(\varepsilon_{F0}\, x^{2/3} \right) \right. = 6.463 \cdot 10^{-5} T_e \left/ x^{2/3} \right., \tag{14}$$

with ε_{F0} being the Fermi energy at normal density $x = 1$. The numerical value for τ (14) corresponds to the temperature T_e measured in Kelvin, density $x = 1$, and Fermi energy $\varepsilon_{F0} = 8$ eV. The energy $\varepsilon_{F0} = 8$ eV corresponds to our DFT calculations of the electron DOS shown in Figs. 1 and 3. Physically the definition (14) represents the electron temperature normalized to the current value of the Fermi energy dependent on the density.

It is known [9], that at low electron temperatures $k_B T_e \ll \varepsilon_F$ the internal energy of the electron subsystem calculated per unit of volume is a power series expansion starting from a term proportional to T_e^2:

$$E_e(T_e, n_e) = \frac{3}{5}\, n_e\, \varepsilon_F \left[\frac{5}{12}\pi^2 \left(\frac{k_B T_e}{\varepsilon_F} \right)^2 + \dots \right], \tag{15}$$

where n_e is the concentration of electrons, the dots referring to higher order terms on the dimensionless temperature $k_B T_e/\varepsilon_F$. We see that the temperature T_e and density n_e variables are inseparable in the expression for the electron energy (15), which means that the function $E_e(T_e, n_e)$ cannot be represented as a product of factors $T(T_e)$ and $N(n_e)$.

Thus, we introduce a variable τ (14) (dimensionless temperature) and search for the electron energy (15) in the form

$$E_e(T_e, n_e) = x^{5/3}\Phi(\tau),\tag{16}$$

where E_e is the electron energy density (12) measured in GPa (1 GPa = 10^9 J/m^3). We use a finite order Pade approximation to describe the function $\Phi(\tau)$ (16):

$$\Phi(\tau) = A_0\tau^2\left(1 + A_1\,\tau + A_2\,\tau^2\right) \big/ \left(1 + B_1\,\tau + B_2\,\tau^2\right).\tag{17}$$

There are five parameters A_0, A_1, A_2, B_1, B_2 in our approximation of electron energy and we adjust these parameters to the DFT data for the electron energy calculated according to (12). The resulting values are

$$A_0 = 47.8807,\ A_1 = 1.066574073,\ A_2 = 0.828076738,\tag{18}$$

$$B_1 = -0.895444194741,\ B_2 = 2.114074407399.$$

A comparison of the electron energy calculated using the DFT approach and the Pade approximation (16), (17), and (18) is shown in Fig. 10, where the crosses represent our DFT simulations described in Section Experimental Design, Materials, and Methods. The errors in the computations are larger at low temperatures. Therefore, we omitted the first data point in Fig. 10 at $T_e = 2$ kK from the DFT dataset used to search for the coefficients (18). We use the asymptotic dependence $\partial E_e/\partial T_e|_V = \gamma T_e$ with γ equal to 400 J/m^3/K in combination with the DFT data to define the coefficients (18). The dependence $E_e(T_e, x = 1)$ (16) based on these coefficients (18) is shown as the red continuous curve in Fig. 10.

The value $\gamma = 400$ J/m^3/K is taken from Ref. [10]. If we use all DFT data points shown in Fig. 10 and approximations (16), (17), then the slope γ at low temperatures T_e will be $\gamma \approx 80$ J/m^3/K. Thus, a moderate decrease from $E_e = 1$ GPa to 0.74 GPa at the point $T_e = 2$ kK in Fig. 10 will decrease the slope 5 times relative to the value $\gamma = 400$ J/m^3/K. The value $E_e = 0.74$ GPa at the temperature $T_e = 2$ kK corresponds to the first data point in Fig. 10, while the value $E_e = 1$ GPa at $T_e = 2$ kK is obtained for the red continuous curve in Fig. 10. If we use the relation $\gamma = (\pi^2/3)\,k_B^2\,g(\varepsilon_F)$ and the value $g(\varepsilon_F) = 0.787$ eV^{-1} atom^{-1} from the electron spectrum in Fig. 3, then $\gamma = 230$ J/m^3/K.
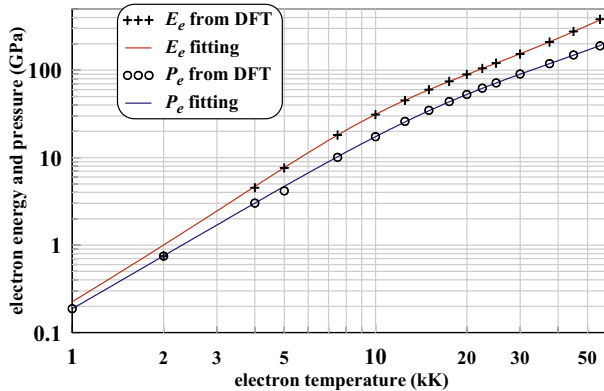
Fig. 10. Careful adjustment of our Pade approximation (16), (17), and (18) of the electron subsystem internal energy to the DFT data. This is done together with adjustment of the electron pressure (19), (20). The curves correspond to normal density Ru. The raw data are provided in Supplementary Materials.

This uncertainty of the slope γ at $T_e < 2$ kK has only a small effect on the energy behavior at temperatures above 2 kK. The energy E_e corresponding to temperature $T_e = 2$ kK is small: ~ 0.1 eV/atom, see Fig. 16. This level of absorbed energy is smaller than the melting threshold and is significantly smaller than the energies needed for ablation. The electron subsystem of Ru is dense, therefore the electron heat capacity $C_e(T_e)$ increases quickly with T_e and becomes comparable with the heat capacity of the crystal lattice ($\approx 3k_B$) already at a temperature of around 4 kK, see Fig. 2.

3.2. Electron pressure and Grüneisen parameter

We use a similar approach to the expansion with Pade approximation (17) to describe the dependence of the electron pressure (13) on the electron temperature and density. A charge neutrality is assumed, thus the electron concentration is defined by the density. The electron pressure equals to

$$p_e(T_e, n_e) = x^{5/3}\Phi(\tau). \tag{19}$$

The same representation is used for the electron energy described above (16). Of course, the coefficients are different for energy and pressure: the coefficients of the approximation (19), (17) for the pressure are

$$A_0 = 44.2226757895, \tag{20}$$

$$A_1 = 0.2519996727, \ A_2 = 0.0913205238175,$$

$$B_1 = 0.03005715652, \ B_2 = 0.61703087.$$

The same definition of the parameter τ (14) (electron temperature normalized to the Fermi energy) is used.

Comparison of our DFT data and the approximation (17), (19), and (20) is presented in Figs. 10 and 11. The original DFT data (black circles in Fig. 11) were shifted down to satisfy the condition $P_e(T_e = 0, x = 1) = 0$. This shift is necessary because the DFT data were obtained for the hcp cell without exact adjustment of the cell size. The density was fixed at $x = 1$ during the variation of temperature T_e. The hexagonal ratio c/a was relaxed at every DFT point.

Fig. 12 demonstrates the influence of relaxation of the hexagonal ratio c/a on the data. The 2T stage in Ru is short, its duration is ~ 1 ps. During this stage the isochoric conditions are approximately fulfilled. Also the duration of the 2T stage is not sufficient for complete relaxation relative to the ratio c/a. Thus, the real situation is somewhere in between the two curves in Fig. 12. The difference between the curves is of the order of 10%.

The electron Grüneisen parameter G_e is the ratio of the electron pressure to the electron energy $G_e = p_e/E_e$ of the partially degenerated electrons. For the Fermi gas this ratio is 2/3 at any temperature as it is for an ideal classical monoatomic gas. Fig. 13 presents the temperature dependence of the parameter G_e for two normalized densities $x = 1$ and $x = 0.8$, $x = \rho/\rho_0$. The dependence for density $x = 1$ directly follows from our DFT data for the electron pressure (Figs. 10 and 11) and electron energy (Fig. 10). The dependence for the decreased density $x = 0.8$ in Fig. 13 is obtained from our Pade-like approximations (16), (17), (18), (19), and (20) based on the Fermi gas approximation and on the DFT data for the normal density $x = 1$.

As one can extract from Fig. 13, the Ru electron subsystem pressure response to the heating is steeper than that of a Fermi-gas system - its Grüneisen parameter shown in Fig. 13 is smaller than the value of 2/3, if we exclude the low temperatures range. At the high electron temperature part the difference
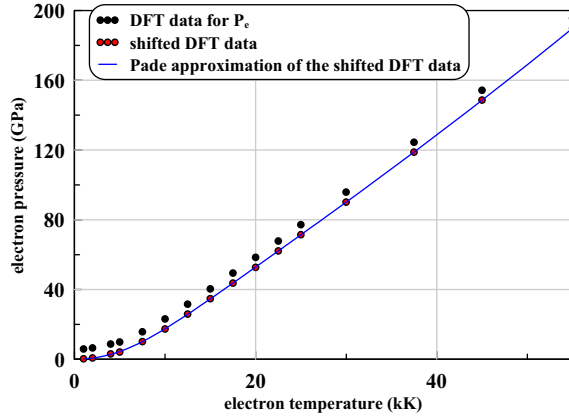
Fig. 11. The blue curve is an approximation of the DFT data for the electron pressure (13) with an analytical dependence (16), (17), and (20). The original DFT data (solid black circles) were shifted down to satisfy the condition $P_e(T_e = 0, x = 1) = 0$. The shifted points are shown by the solid red circles. The raw data are provided in Supplementary Materials.
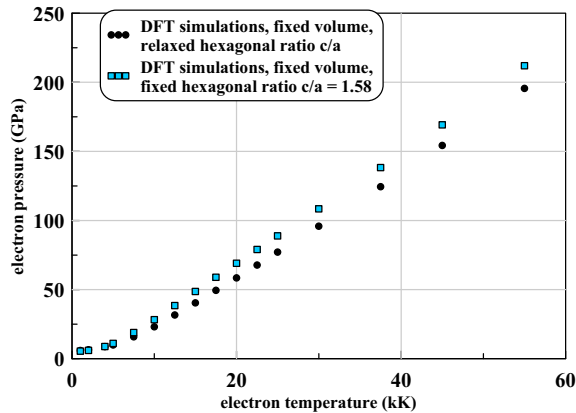
Fig. 12. In both cases shown here the electron pressure was calculated at different temperatures T_e and a fixed volume $x = 1$. In the first case the height to base ratio c/a was fixed, while in the second case this ratio was relaxed at every value of the temperature T_e. The black circles relate to the second case. The second case also is presented by the same circles in Fig. 11. Obviously, relaxation decreases pressure. The raw data are provided in Supplementary Materials.

between the two curves can be explained by the energy expenses required for the ionization of 4p-electrons, see Fig. 2 for the electron heat capacity and the discussion about this feature in Section 1.1.2.

3.3. Dependencies of electron energy and pressure on density

The density dependencies of the electron energy and pressure described with the Pade approximations (16), (17), (18), (19), and (20) are shown in Figs. 14 and 15. These dependencies react moderately to a variation of the density. Even a factor of two reduction of the density leads to a moderate decrease of the electron energy and pressure:

$$\frac{E_e(2\ \text{eV}, 1)}{E_e(2\ \text{eV}, 0.5)} = 1.7, \quad \frac{E_e(1\ \text{eV}, 1)}{E_e(1\ \text{eV}, 0.5)} = 1.6,$$
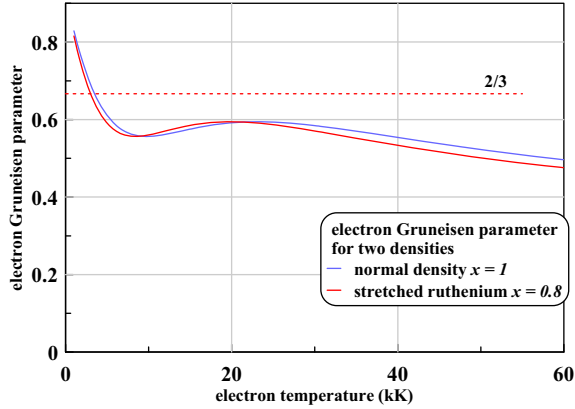
Fig. 13. Dependence of electron Grüneisen parameter on electron temperature and density.
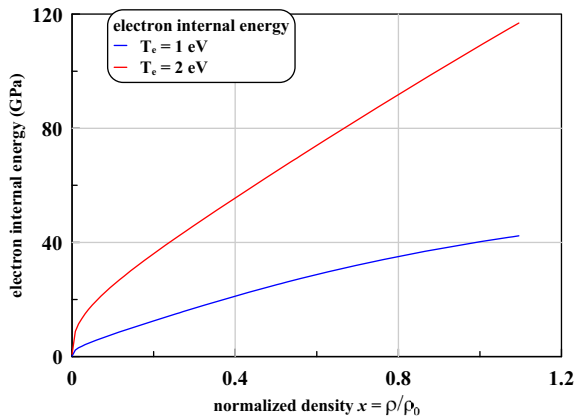

Fig. 14. Dependence of electron energy on density. We see that energy moderately decreases at moderate stretching typical for the 2T stage in our range of absorbed energies. The raw data are provided in Supplementary Materials.

$$\frac{p_e(2\,\text{eV}, 1)}{p_e(2\,\text{eV}, 0.5)} = 1.8, \quad \frac{p_e(1\,\text{eV}, 1)}{p_e(1\,\text{eV}, 0.5)} = 1.5.$$

We emphasize again that during the 2T stage only a limited variation of the density takes place, because this stage is short ~ 1 ps.

Above, in expression (16) and in Fig. 10, the electron energy is described as energy per unit of volume. Fig. 16 shows this energy per unit of mass. A transformation rule is: $1\,\text{GPa} \rightarrow 0.084/x$ eV/atom, where x is the normalized density. The volumetric density of electron energy depends weakly on variation of the density, see Fig. 14. Therefore, the stretching moderately increases the electron energy per unit of mass, see Fig. 16.
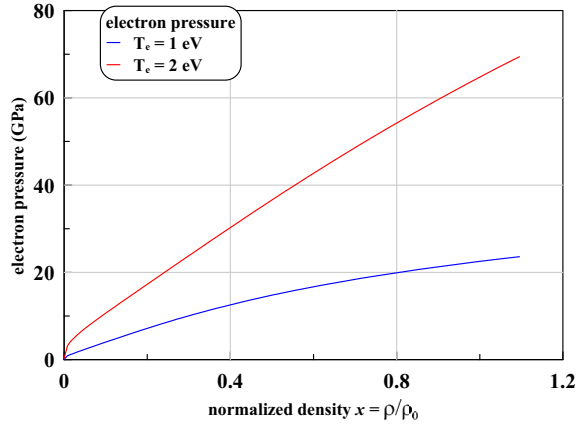
Fig. 15. Influence of stretching on electron pressure. As in the case with electron energy in previous Fig. 14 the electron pressure is moderately sensitive to stretching. The raw data are provided in Supplementary Materials.
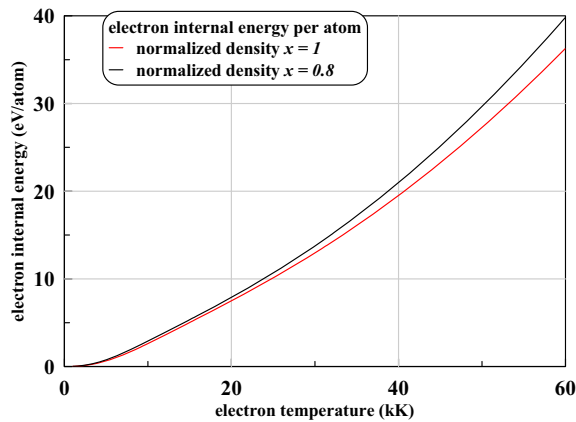

Fig. 16. Electron energy calculated per atom for two densities. The raw data are provided in Supplementary Materials.

4. Kinetic coefficients in one- and two-temperature Ru

4.1. Conductivity and electron-electron processes

The rate of diffusion of electrons transporting charge and heat depends on the collision frequency ν. At normal conditions (room temperature) electron-ion scattering dominates over electron-electron scattering, since electrons are strongly degenerated.

In the 2T regime the electron temperatures T_e are high. The concentration of electrons n_e ($k_B T_e / \varepsilon_{F0}$) in a temperature layer around the Fermi level increases, and the electron-electron scattering becomes significant and even overcomes the electron-ion scattering, see Refs. [11–13]. The electron-electron contribution is usually described within the approximation, where the frequency ν_{ee} of electron-electron collisions is proportional to T_e^2.

In reality the fast growth of the frequency $\nu_{ee} \propto T_e^2$ saturates rather early, at moderate values of electron temperatures [3,11], similar to a situation when a linear growth of electron heat capacity $C_e =$

γT_e turns into a non-linear dependence, see e.g., Fig. 2. The deviation from the dependence $\nu_{ee} \propto T_e^2$ influences very significantly the 2T electron thermal conductivity κ.

One of the widely used approximation [12] for the conductivity κ is

$$\kappa = C \, \frac{(\theta^2 + 0.16)^{5/4} (\theta^2 + 0.44)\theta}{(\theta^2 + 0.092)^{1/2} (\theta^2 + b \, \theta_i)}, \tag{21}$$

where θ and θ_i are the electron and the ion temperatures normalized to the Fermi energy, C and b are material dependent constants. Approximation (21) is based on the free electron gas model and can be simplified if one considers particular temperature regimes: firstly, at low temperatures it tends to the well-known limit $\kappa \propto T_e/T_i$; secondly, in the intermediate range of temperatures T_e the corresponding collision frequency behaves as $A \, T_i + B \, T_e^2$, [11,12]; and, thirdly, for very high temperatures T_e the approximation (21) scales as $T_e^{5/2}$ with temperature T_e (plasma limit) [11].

Another popular approximation [12] is

$$\kappa = (1/3)\nu_F^2 \, C_e \Big/ \left(A \, T_i + B \, T_e^2 \right), \tag{22}$$

where ν_F is the Fermi velocity, and C_e is the electron heat capacity.

In the present approach we use a parabolic approximation [3,11,13,14] of the electron DOS (see Fig. 3). In the calculations of thermal conductivity we use the solution of the Boltzmann equation in the relaxation time approximation [3,11] and the geometrical distribution of the DOS presented as the Fermi sphere of s-electrons overlapping in the momentum space with a spherical layer of d-electrons. The s-sphere occupies the range of s-electron energies $0 < \varepsilon_s < \varepsilon_F$, while the d-layer is located in the shell $\varepsilon_1 < \varepsilon_d < \varepsilon_2$ [3,11].

Results obtained for the conductivity κ strongly deviate from approximations (21) and (22) at elevated electron temperatures. The approximations (21), (22) significantly suppress values of κ, because they overestimate the frequency of electron-electron collisions [11].

Another drawback of the approximations (21) and (22) is that they do not include the s- and d-band separately. In our theory we consider these bands as connected, but independent entities. They are connected through the normalization condition $\int g_s f + \int g_d f = z_s + z_d$, where g_s, g_d are partial densities of states of the s- and d-band electrons, f is the Fermi distribution, z_s, z_d are numbers of s- and d-electrons per atom in the conduction band; $z_s = 1$, $z_d = 7$ for Ru $4d^7 5s^1$. This condition is used to define the dependence of the chemical potential on the electron temperature. After that the partial thermal capacities are calculated. The s-band electrons give the main contribution to the transport of heat and charge. The effective masses of s- and d-electrons are calculated using the two-parabolic approximation, see Fig. 3. The obtained values are $m_s = 0.88 m_e$ and $m_d = 3.62 m_e$.

4.2. Calculation of electron-electron scattering

The total thermal conductivity κ is defined by electron-ion and electron-electron processes. Combining these processes we write

$$\kappa = (1/\kappa_{si} + 1/\kappa_{se})^{-1}, \tag{23}$$

where κ_{si} and κ_{se} are partial contributions.

As written above, at not too high electron temperatures T_e the term κ_{se} in (23) is

$$\kappa_{se} = \left(\pi^2 \big/ 6\right) n_s k_B \, (k_B T_e \big/ \varepsilon_F) \nu_F^2 \big/ \nu_{se}. \tag{24}$$

For small values of T_e we have

$$\nu_{\text{se}} \propto (\varepsilon_{\text{F}} / \hbar) \, (k_{\text{B}} \, T_{\text{e}} / \varepsilon_{\text{F}})^2.$$

Therefore

$$\kappa_{\text{se}} \propto \frac{\hbar \, k_{\text{B}}}{m_s} \, n_s \, \frac{\varepsilon_{\text{F}}}{k_{\text{B}} \, T_{\text{e}}} \propto x \, \frac{1}{\tau}, \tag{25}$$

where $x = \rho/\rho_0$ and τ is defined by the expression (15). In formula (25) the term proportional to the density x comes from the electron thermal capacity per unit of volume in the Drude model (24) for thermal conduction. The dependence on τ in (25) appears as a result of dividing the temperature dependent heat capacity by the temperature dependent collision frequency in (24).

Formula (25) leads us to the idea to look for the dependence of the thermal conductivity on density and temperature in the form of a product:

$$\kappa_{\text{se}}(T_e, x) = x \, Q_{se}(\tau), \tag{26}$$

where τ is the normalized temperature $\tau = 6 \, k_{\text{B}} \, T_e / \varepsilon_{\text{F}}$ (14), and $\varepsilon_{\text{F}} = \varepsilon_{\text{F0}} \, x^{2/3}$ is a quantity depending on the normalized density.

The electron thermal conductivity κ_{se} is defined as the sum of two partial thermal conductivities

$$\kappa_{\text{se}}^{-1} = \kappa_{\text{ss}}^{-1} + \kappa_{\text{sd}}^{-1},$$

because the heat transfer by s-electron slows down due to scattering on both s- and d-electrons.

The conductivities κ_{ss} and κ_{sd} are calculated at $x = 1$ for many different electron temperatures T_e covering a wide range of values T_e. To simplify the 2T-HD code, the obtained data $\kappa(T_e, x = 1)$ are approximated by an analytical fit

$$Q_{se}(\tau) = 10^3 \frac{1 + 0.4017\tau + 1.7877\tau^2 + 0.3725\tau^3}{\tau(25.123 + 0.2524\tau)}, \tag{27}$$

where Q_{se} is measured in W/m/K. This fit (27) and equation (26) define the contribution of the electron-electron scattering to the conductivity. The Pade approximation (27) has a right asymptotic dependence (25) at low temperatures τ.

4.3. Calculation of electron-ion scattering

Thermal conductivity due to electron-ion scattering can be written as

$$\kappa_{\text{si}} = \frac{1}{3} C_s(T_e, x) \nu_s(T_e, x) \lambda_{\text{si}}(T_i, x). \tag{28}$$

Expression (28) follows from the Drude model. In (28) C_s is the s-electron heat capacity per unit volume, $\nu_s(T_e, x)$ is the velocity of s-electrons transporting heat along a temperature gradient. The term $\lambda_{\text{si}}(T_i, x)$ represents a mean free path of s-electrons between the events of collisions with ions.

As written at the end of Section 4.1, we use the normalization condition $\int g_s f + \int g_d f = z_s + z_d$ to find the electron chemical potential $\mu(T_e)$, its derivative $\partial \mu / \partial T_e$, the internal energy of s-electrons, and the heat capacity of s-electrons C_s per unit of volume. We present the capacity C_s as a function $C_s = n_s \, k_{\text{B}} \, f_1(\tau)$, where τ is given by expression (14). The mean electron velocity $\nu_s(T_e, x)$ can be written as

$$\nu_s = \nu_{\text{F}}(x) \sqrt{1 + 3k_{\text{B}}T_e / (2\varepsilon_{\text{F}}(x))},$$

with ν_{F} being a Fermi velocity. We see that the product $C_s \, \nu_s$ can be expressed as

$$C_s \, v_s(T_e, x) = x^{4/3} C(\tau). \tag{29}$$

The product $C_s \, v_s$ and consequently the function $C(\tau)$ calculated with these spectral parameters at $x = 1$ for a set of temperatures T_e is analytically fitted with the expression

$$C(\tau) = \frac{\tau \, (1 + 0.2704 \, \tau^2)}{1 + 0.1991 \, \tau^{1.9371}}. \tag{30}$$

The mean free path λ_{si} is

$$\lambda_{si} = 1 \, / \, (n\sigma),$$

where n is an ion concentration and σ is an electron-ion scattering cross section. The cross section equals to

$$\sigma \propto u_t^2 \propto u_0^2 T_i \big/ \theta_D,$$

with u_0^2, u_t^2 being the mean squared amplitude of zero-point and thermal lattice vibrations, respectively, θ_D is the Debye temperature. Here we make no distinction between acoustical and optical vibrational modes at ion temperatures T_i under consideration, exceeding the Debye temperature θ_D. The hcp lattice of Ru has three acoustical and three optical vibrational modes because there are two atoms in a unit cell of a crystal.

Considering that

$$u_0^2 \propto \frac{\hbar^2}{M \, k_B \, \theta_D}$$

(M is mass of an atom), we have

$$\sigma \propto \frac{\hbar^2}{M \, k_B \, \theta_D} \, \frac{T_i}{\theta_D} \propto \frac{T_i}{\theta_D^2},$$

and then

$$\lambda_{si} \propto \frac{(\theta_D(x))^2}{x \, T_i} \propto \frac{y_0(x)}{x^{1/3} \, T_i}. \tag{31}$$

Here we use expression (10) to derive the dependence of the mean free path λ_{si} on the density. Expression (10) connects the Debye temperature with the cold curve for pressure (2), which determines the stiffness of the lattice.

Substituting $C_s \, v_s$ (29) and λ_{si} (31) into the Drude model (28) we obtain an expression for the electron-ion contribution to the thermal conductivity

$$\kappa_{si}(T_e, T_i, x) \propto x \, y_0(x) \, C(\tau) \, / \, T_i.$$

Let's normalize this expression knowing the room temperature (rt) value of the thermal conductivity $\kappa_{si}(T_{rt}, T_{rt}, 1) = \kappa_{rt} = 117$ W/m/K. Then we have

$$\kappa_{si}(T_e, T_i, x) = \kappa_{rt} x (y_0(x) \, / \, y_0(1))(C(\tau) \, / \, C(\tau_{rt}))(T_{rt} \, / \, T_i).$$

Substituting here the values $y_0(1) = 1$ [Eq. (9)], $T_{rt} = 300$ K, $\tau_{rt} = 0.0194$ [Eq. (14)], $C(\tau_{rt}) \approx \tau_{rt}$ [Eq. (30)], we obtain

$$\kappa_{\text{si}}(T_e, T_i, x) = 1.8 \cdot 10^6 x y_0(x) C(\tau) \big/ T_i. \tag{32}$$

The conductivity (32) is measured in W/m/K. We see that it quickly decreases as the density decreases $\propto x^{2a+4/3} \approx x^{4.5}$ (in solid state), and behaves approximately $\propto T_e$ as in the frequently used approximation $\kappa_{si} = \kappa_{rt} T_e/T_i$. At $x = 1$ the expression (32) is very close to the dependence $T\kappa_{si} = \kappa_{rt} T_e/T_i$.

4.4. Total two-temperature thermal conductivity

Electron-ion and electron-electron resistance both slow down transport of heat by s-electrons. A sum of the resistances is

$$\kappa(T_e, T_i, x) = 1 / (1 / \kappa_{si} + 1 / \kappa_{se}), \tag{33}$$

where partial contributions are defined by expressions (32) and (26). These partial contributions and the inverse sum of their resistances are presented in Fig. 17. At low temperatures T_e the temperature layer around a Fermi level is narrow, almost all electrons are degenerated, thus an electron-electron collision frequency is small. In this case electron-ion scattering defines conductivity κ, while for elevated temperatures T_e (T_i is fixed) electron-electron scattering defines conductivity κ. Fig. 18 shows how the conductivity κ (33) decreases with increase of the ion temperature.

4.5. Electron-phonon coupling factor

The energy transferred from the electron to the ion subsystem per unit time and per unit volume at $T_e > T_i$ within the Kaganov-Lifshitz-Tanatarov theory [15] is given by the expression:

$$\frac{\partial E}{\partial t}_{e-ph} = \alpha(T_e)(T_e - T_i), \tag{34}$$

where the coefficient $\alpha(T_e)$ is known as the electron-phonon coupling factor. We calculate $\alpha(T_e) = \alpha_s(T_e) + \alpha_d(T_e)$ taking into account the heat transfer to the ions separately from s- and d-electrons, using the formalism described in Ref. [3]:
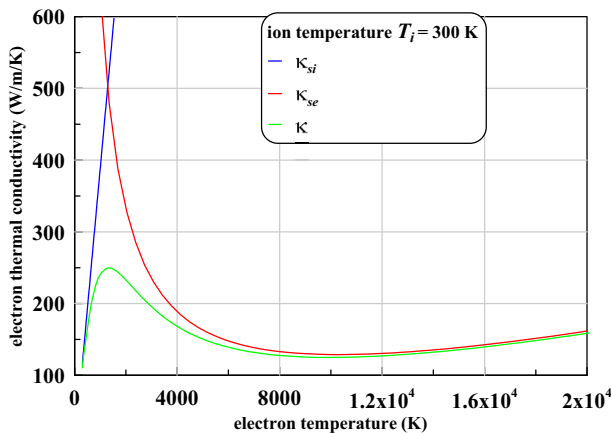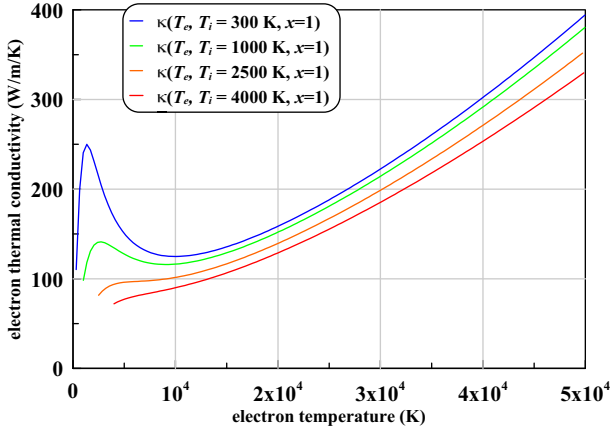

Fig. 17. The total thermal conductivity $\kappa(T_e, T_i = 300\,\text{K}, x = 1)$ and its components κ_{si} and κ_{se}.

Fig. 18. Conductivities κ calculated according to expression (33) for different ion temperatures T_i equal to 300, 1000, 2500, and 4000 K.

$$\alpha_s(T_e) = \frac{m_s^2}{4\pi^3\hbar^7}\frac{k_B^2 T_e}{\rho_0 c_s}\int\limits_0^{q_D} dq q^2 U^2(\mathbf{q})$$

$$\ln\left(\frac{\exp\left(\frac{(q/2+m_s c_s)^2/(2m_s)-\mu-\hbar\omega_q}{k_B T_e}\right)+1}{\exp\left(\frac{(q/2+m_s c_s)^2/(2m_s)-\mu-\hbar\omega_q}{k_B T_e}\right)+\exp\left(\frac{-\hbar\omega_q}{k_B T_e}\right)}\right), \tag{35}$$

$$\alpha_d(T_e) = \frac{m_d^2}{4\pi^3\hbar^7}\frac{k_B^2 T_e}{\rho_0 c_s}\int\limits_0^{q_D} dq q^2 U^2(\mathbf{q})$$

$$\left[\ln\left(\frac{\exp\left(\frac{E_{max}-\mu-\hbar\omega_q}{k_B T_e}\right)+\exp\left(\frac{-\hbar\omega_q}{k_B T_e}\right)}{\exp\left(\frac{E_{max}-\mu-\hbar\omega_q}{k_B T_e}\right)+1}\right)- \right.$$

$$\left.-\ln\left(\frac{\exp\left(\frac{E_{min}-\mu-\hbar\omega_q}{k_B T_e}\right)+\exp\left(\frac{-\hbar\omega_q}{k_B T_e}\right)}{\exp\left(\frac{E_{min}-\mu-\hbar\omega_q}{k_B T_e}\right)+1}\right)\right]. \tag{36}$$

Here, q is the absolute value of the phonon momentum, q_D is the Debye momentum, $\omega_q = c_s q/\hbar$ is the phonon dispersion relation written in the Debye approximation, $\mu = \mu(T_e)$ is the chemical potential. E_{min} and E_{max} are defined as:

$$E_{min} = \varepsilon_1 + \frac{1}{2m_d}\left(\frac{q}{2}+m_d c_s\right), \ E_{max} = \varepsilon_1 + \frac{p_d^2}{2m_d}, \tag{37}$$
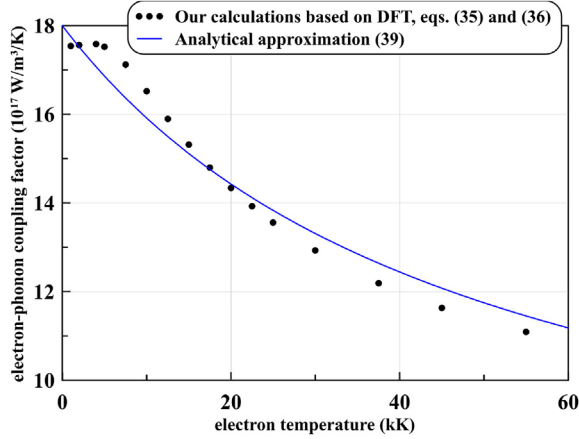
Fig. 19. Electron−phonon coupling factor as a function of electron temperature. The raw data are provided in Supplementary Materials.

where momentum $p_d = \sqrt{2m_d(\varepsilon_2 - \varepsilon_1)}$, and ε_1 and ε_2 are introduced in Fig. 3. The effective masses of s- and d-electrons m_s and m_d, respectively, are defined in Section 4.1.

The Fourier transform of the screened Coulomb potential $U(\mathbf{q})$ is defined as (see Ref. [3] for the details):

$$U(\mathbf{q}) = 4\pi e^2 \hbar^2 Z_i n_a t \left/ q^2 \varepsilon(\mathbf{q}) \right., \tag{38}$$

where Z_i is the effective charge number of the ion and $\varepsilon(\mathbf{q})$ is the dielectric constant, which is calculated in the Singwi-Sjolander approximation [16]. Since it is known that the speed of sound c_s can be dependent on the electron temperature, we performed series of DFT calculations to obtain such a dependence. We found that it can be approximated by an expression $c_s(T_e) = 7.25 + 0.2T_e$ km/s, where T_e is in eV. Such dependence has an insignificant effect on the electron phonon coupling factor for T_e below 20000 K.

We do not take into account the dependence of α on the ion temperature T_i. Such approximation is accurate for ion temperatures much higher than the Debye temperature (555 K for Ru, [17]). The dependence on the density is also neglected, since the 2T stage in Ru is short and the density does not change significantly during that stage.

The integrals 35 and 36 are solved numerically for different electron temperatures T_e. The data are fitted by

$$\alpha(T_e) = \left(18 - \frac{12.5 * T_e}{50 + T_e} \right) \tag{39}$$

where T_e is in [kK] units and α is in 10^{17}W/m^3/K. Such a simple dependence shown in Fig. 19 is used in our 2T-HD calculations of Ru irradiated by ultrafast laser pulses.

5. Summary

We summarize the work presented above with the list of expressions for the equations of state and the kinetic coefficients (electron thermal conductivity and electron-phonon coupling factor) that we use in our 2T-HD calculations [1].

- Internal energy of ion subsystem: (4) and (3);
- Pressure of ion subsystem: (5), (3) and (11);

- Internal energy of electron subsystem: (16), (17), (18) and (14);
- Pressure of electron subsystem: (19), (17), (20) and (14);
- Electron thermal conductivity: (23), (26), (27), (32), (9), (30) and (14);
- Electron−phonon coupling factor: (39).

6. Experimental design, materials, and methods

Calculations based on the density functional theory (DFT) are performed using the projector augmented wave (PAW) method within the Vienna *ab initio* simulation package (VASP) [18]. Some data obtained with PAW were cross-checked using the linearized augmented-plane wave (LAPW) method carried out with the help of the Elk code [19]. We consider the primitive cell of Ru corresponding to the stable hexagonal close-packed (hcp) lattice with periodical boundary conditions.

In our PAW calculations, the maximum energy of one-electron wavefunctions was fixed at 400 eV, the density of the Monkhorst-Pack grid was set equal to $21 \times 21 \times 21$ and the number of empty electron levels per atom was equal to 32. During all-electron calculations using the Elk code [19], we set the product of the muffin-tin radius and a maximum of electron quasi-momentum beyond the sphere with the muffin-tin radius equal to 10.0 and use the same density of the Monkhorst-Pack grid. In our PAW and LAPW calculations we describe exchange and correlation contributions in electron-electron interaction with PBE functional, which is a simplified generalized gradient approximation (GGA) [20].

First of all, with DFT simulations we obtain the so called "cold curves" of Ru, which are the dependencies of pressure and internal energy on density at absolute zero electron and ion temperatures. These curves are used to define the cold additions to pressure, $P_i^{cold}(\rho)$, and internal energy, $\varepsilon_i^{cold}(\rho)$, in the Mie-Grüneisen equation of state. We develop analytical approximations of these functions (Section 2.1) to be used in the two-temperature hydrodynamic (2T-HD) simulations. Thermal additions to the ion internal energy and ion pressure are also obtained (Section 2.3).

As a next step, we define the density of states (DOS, electron spectrum) of Ru. To reproduce electron thermodynamics properly at high electron temperatures, we consider not only the conduction band electrons $4d^7 \, 5s^1$, but also electrons from the lower shells $4s^2$ and $4p^6$ (semicore electrons). They are included in the form of the PAW pseudopotential that we use. The effect of the semicore electrons is taken into account by using the extended *sv* form of the PAW datasets for Ru provided in the VASP package, which includes the semicore electrons in the same basis of plane waves as for the conduction electrons.

Finally, the internal energy of the electron subsystem, electron entropy and pressure (PAW calculations) are computed at different electron temperatures T_e for fixed volumes. During these calculations, ions are fixed in their equilibrium positions, thus ion temperatures are $T_i = 0$. The initial lattice constants are $a = b = 2.68$ Å and $c = 1.5789 \, a$ at $T_e = 1000$ K. These lattice parameters correspond to a density of 12.7 g/cm^3.

Acknowledgements

the Czech Ministry of Education, Youth and Sports, Czech Republic [grants numbers LTT17015, LM2015083].

Conflict of Interest

The authors declare that they have no known competing financial interests or personal relationships that could have appeared to influence the work reported in this paper.

Appendix A. Supplementary data

Supplementary data to this article can be found online at https://doi.org/10.1016/j.dib.2019.104980.

References

[1] I. Milov, V. Lipp, D. Ilnitsky, N. Medvedev, K. Migdal, V. Zhakhovsky, V. Khokhlov, Yu Petrov, N. Inogamov, S. Semin, et al., Similarity in ruthenium damage induced by photons with different energies: from visible light to hard x-rays, Appl. Surf. Sci. 501 (2020), 143973.

[2] P.R. Levashov, G.V. Sin'ko, N.A. Smirnov, D.V. Minakov, O.P. Shemyakin, K.V. Khishchenko, Pseudopotential and full-electron dft calculations of thermodynamic properties of electrons in metals and semiempirical equations of state, J. Phys. Condens. Matter 22 (50) (2010) 505501–505510.

[3] Yu V. Petrov, N.A. Inogamov, K.P. Migdal, Thermal conductivity and the electron-ion heat transfer coefficient in condensed media with a strongly excited electron subsystem, JETP Lett. (Engl. Transl.) 97 (1) (2013) 20–27.

[4] A.V. Lugovskoy, M.P. Belov, O.M. Krasilnikov, Yu Kh Vekilov, Stability of the hcp ruthenium at high pressures from first principles, J. Appl. Phys. 116 (10) (2014) 103507.

[5] L.A. Girifalco, Statistical Physics of Materials, first ed., Wiley, 1973.

[6] J.R. Chelikowsky, C.T. Chan, S.G. Louie, Theoretical study of the electronic, structural, and cohesive properties of ruthenium, Phys. Rev. B 34 (10) (1986) 6656–6661.

[7] R. Ramji Rao, A. Ramanand, Lattice dynamics, thermal expansion, and bulk modulus of ruthenium, J. Low Temp. Phys. 27 (5–6) (1977) 837–850.

[8] Y.V. Petrov, K.P. Migdal, N.A. Inogamov, V.V. Zhakhovsky, Two-temperature equation of state for aluminum and gold with electrons excited by an ultrashort laser pulse, Appl. Phys. B 119 (3) (2015) 401.

[9] L.D. Landau, E.M. Lifshitz, Statistical Physics, third ed., Butterworth-Heinemann, 2013.

[10] C. Kittel, Introduction to Solid State Physics, eighth ed., John Wiley & Sons, Inc., New York, 2005.

[11] N.A. Inogamov, Yu V. Petrov, Thermal conductivity of metals with hot electrons, J. Experim. Theor. Phys. (JETP) 110 (3) (2010) 446–468.

[12] Baerbel Rethfeld, Dmitriy S. Ivanov, Martin E. Garcia, Sergei I. Anisimov, Modelling ultrafast laser ablation, J. Phys. D Appl. Phys. 50 (19) (apr 2017), 193001.

[13] K.P. Migdal, V.V. Zhakhovsky, A.V. Yanilkin, YuV. Petrov, N.A. Inogamov, Transport properties of liquid metals and semiconductors from molecular dynamics simulation with the kubo-greenwood formula, Appl. Surf. Sci. 478 (2019) 818–830.

[14] Yu V. Petrov, K.P. Migdal, N.A. Inogamov, S.I. Anisimov, Transfer processes in a metal with hot electrons excited by a laser pulse, JETP Lett. (Engl. Transl.) 104 (6) (Sep 2016) 431–439.

[15] M.I. Kaganov, E.M. Lifshitz, L.V. Tanatarov, Relaxation between electrons and the crystalline lattice, J. Exp. Theor. Phys. 4 (1957) 173–178.

[16] K.S. Singwi, M.P. Tosi, R.H. Land, A. Sjölander, Electron correlations at metallic densities, Phys. Rev. 176 (2) (1968) 589.

[17] C.Y. Ho, B.W. Powell, P.E. Liley, Thermal conductivity of the elements: a comprehensive review, J. Phys. Chem. Ref. Data 3 (1) (1974).

[18] G. Kresse, J. Furthmuller, Efficient iterative schemes for ab initio total-energy calculations using a plane-wave basis set, Phys. Rev. B 54 (1996) 11169.

[19] available for free at http://elk.sourceforge.net, elk. an all-electron full-potential linearized augmented planewave plus local orbitals [fp-(l)apw + lo] code.

[20] J.P. Perdew, K. Burke, M. Ernzerhof, Generalized gradient approximation made simple, Phys. Rev. Lett. 77 (1996) 3865–3868.